Monolithic integrated emitting-detecting configuration based on strained Ge microbridge

Senbiao Qin, Junqiang Sun,* Jialin Jiang, Yi Zhang, Ming Cheng, Linfeng Yu, Kang Wang, Li Kai, Haotian Shi and Qiang Huang

Wuhan National Laboratory for Optoelectronics, School of Optics and Electronic Information,
Huazhong University of Science and Technology, Wuhan 430074, China
*Corresponding author: Junqiang Sun, E-mail: jqsun@hust.edu.cn

This file contains:

1. Ion implantations

BF$_2^+$ and P$^+$ implantations are performed to construct the lateral p-i-n junctions. Implantation parameters are listed in Table S1. As shown in Fig. S1, the concentrations of active dopants present Gaussian distribution for both n-type and p-type. After the annealing process, the active concentration in the p-region is on the order of 10^{20} cm^{-3}. For the p-region, the high diffusivity of phosphorus in Ge limits the active concentration to the order of 10^{19} cm^{-3} [1].

Figure S1. Active dopants concentration (logarithmic scale).

Table S1. Parameters of BF$_2^+$ and P$^+$ implantations

Ion	Implanted dose/cm^{-2}	Energy/keV	Angle/°	Projected Range/nm	Junction depth/nm
BF$_2^+$ (p-type doping)	2×10^{15}	50	7	40	200
P$^+$ (n-type doping)	2×10^{15}	40	7	40	200

2. Strain characterization

X-ray diffraction (XRD) and Raman spectroscopy are performed for characterization of the strain. Figure S2(a) shows the X-ray rocking curve of the as-grown Ge <004> lattice planes, with a Ge peak locating at 66.107° and a full width at half maximum (FWHM) of 0.0817°. The biaxial tensile strain in the as-grown Ge layer is determined form the location of the Ge peak in the X-ray rocking curve. For the given Ge <004> lattice planes with an inter-plane distance of d_{004}, the condition for a diffraction peak to occur can be determined by the Bragg's law:

$$2d\sin\theta = n\lambda \tag{S1}$$

where θ is the diffraction angle. n is an integer representing the order of the diffraction peak. λ = 0.15406 nm is the wavelength of the X-ray. A diffraction peak of Ge locating at 2θ = 66.107° represents an inter-plane distance of 1.4123 Å. Due to the tetragonal crystal structure, the inter-plane distance of the <001> crystal orientation d_{001} can be derived as follows:

$$d_{hkl}{}^{2} = \frac{1}{\left(h^{2}+k^{2}+l^{2}\right)} \times d_{001}{}^{2} \tag{S2}$$

Here, h, k and l are Miller indices. d_{001} = 5.6492 Å, indicating a compressive strain of 0.156% in the z direction comparing with the lattice constant of 5.658 Å in the relaxed Ge layer. The relationship between strain components of ε_{xx}, ε_{yy} and ε_{zz} can be described as the following equations:

$$\varepsilon_{xx} = \varepsilon_{yy} \tag{S3}$$

$$\varepsilon_{zz} = -\frac{2C_{12}}{C_{11}}\varepsilon_{xx} \tag{S4}$$

Here, elastic constants C_{11} and C_{12} are 128.53 GPa and 48.26 GPa in the Ge layer, respectively.

Raman spectroscopy results for the as-grown Ge and Ge microbridges with etching time of 15 min and 20 min are shown in Fig. S2(b), with Raman intensity peaks locating at 307.9 cm^{-1}, 306.2 cm^{-1} and 304.5 cm^{-1}, respectively. The relationship between the location of the Raman spectra and the strain value in Ge layer has been explored in ref. [2]:

$$\varepsilon = a\times\Delta\omega + b\times\Delta\omega^{2} \tag{S5}$$

Here, a and b are coefficients with different values for biaxial and uniaxial tensile strain (see Table S2).

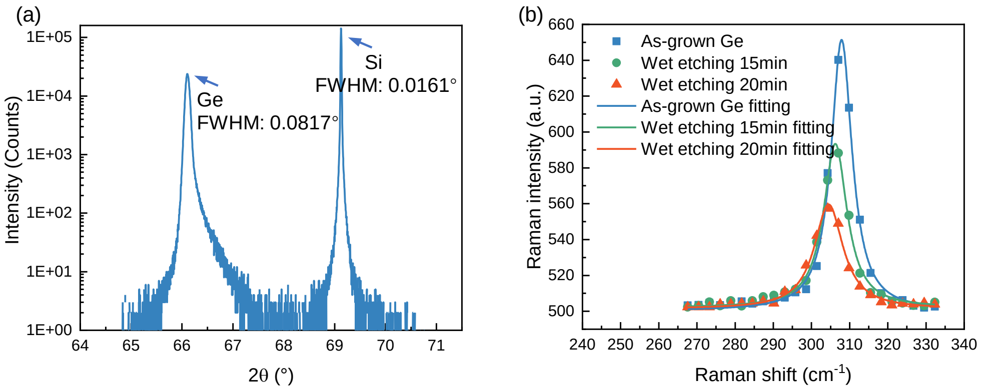

Figure S2. (a) The X-ray rocking curve of the as-grown Ge <004> lattice planes. The marked Ge peak is located at 66.107° with a full width at half maximum (FWHM) of 0.0817°. (b) The Raman spectroscopy of the as-grown Ge and Ge microbridge with wet etching of 15 min and 20 min for suspension. The Raman intensity peaks calculated by Lorentz fitting are located at 307.9 cm^{-1}, 306.2 cm^{-1} and 304.5 cm^{-1}, respectively.

The Raman peak of the relaxed bulk Ge was reported to be located at 301.1 cm^{-1}, and the peak location of strained Ge should be smaller than relaxed Ge [2]. There is a deviation between the test result and the reported value, which results from the uncalibrated Raman spectroscopy system. Here, data of XRD and Raman spectroscopy for as-grown Ge layer are compared to measure such deviation. The flow chart of the calibration of Raman spectroscopy system and strain calculation is shown in Fig. S3. The deviation is 7.7 cm^{-1}. The calibrated Raman peak locations of Ge microbridges with different wet etching time of 15min and 20min are 298.5 cm^{-1} and 296.8 cm^{-1}, corresponding to relative Raman shifts of 2.6 cm^{-1} and 4.3 cm^{-1}. According to Eq. S5, the values of uniaxial tensile strain of the two different Ge microbridges are 1.6% and 2.6%.

Table S2. Coefficients in strain characterization with Raman spectroscopy

Strain type	a	b
Biaxial tensile strain in x-y plane	0.23	0
Uniaxial tensile strain in the lattice orientation of <100>	0.68	-0.019

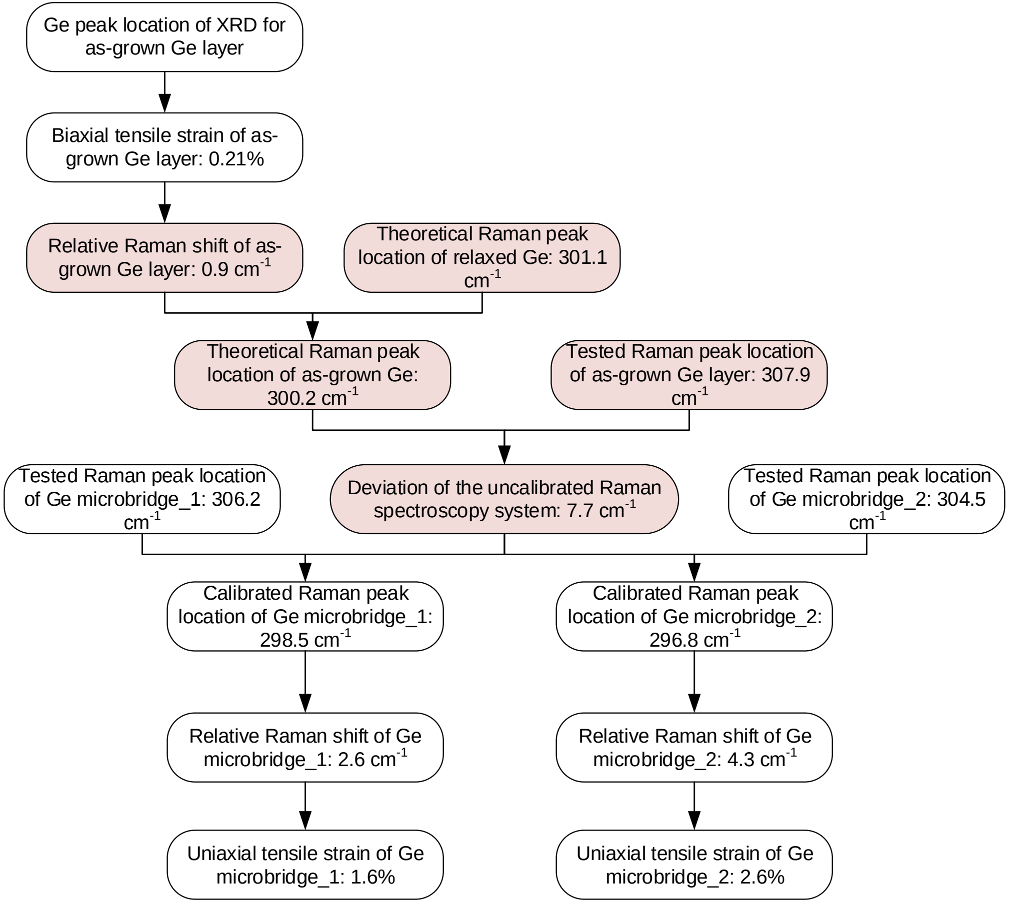

Figure S3. Flow chart of strain calculation and calibration of Raman spectroscopy system.

3. Joint density of state (JDOS) model

The spontaneous emission rate and interband absorption spectra are calculated by the joint density of state (JDOS) model:

$$r^{spon}(\hbar\omega)=\left(\frac{n_r^{2}\omega^{2}}{\pi^{2}\hbar c^{2}}\right)C_0\left|\hat{e}\cdot p_{cv}\right|^{2}\rho_r\left(\hbar\omega-E_g\right)f_c\left(1-f_v\right) \tag{S6}$$

$$C_0 = \frac{\pi e^2}{n_r c \varepsilon_0 m_0^2 \omega} \tag{S7}$$

$$\rho_r\left(\hbar\omega - E_g\right) = \frac{1}{2\pi^2}\left(\frac{2m_r^*}{\hbar^2}\right)^{3/2}\left(\hbar\omega - E_g\right)^{1/2} \tag{S8}$$

$$\alpha\left(\hbar\omega\right) = C_0\left|\hat{e}\cdot p_{cv}\right|^2 \rho_r\left(\hbar\omega - E_g\right) \tag{S9}$$

where n_r is the refractive index. ω is the angular frequency of the photon. $\hbar$ is the reduced Planck constant. c is the light speed in the vacuum. e and m_0 are the electron charge and mass, respectively. ε_0 is the permittivity in the vacuum. m_r is the reduced mass of electrons in conduction band. E_g is the bandgap. $\left|\hat{e}\cdot p_{cv}\right|$ is the momentum matrix element. $\rho_r\left(\hbar\omega - E_g\right)$ represents the joint density of state. f_c and f_v are the Fermi-Dirac functions of the conduction band and valence band, respectively. Both transitions for Γ-HH and Γ-LH have to be taken into consideration.

4. Theoretical spontaneous emission and absorption spectrum

To theoretically analyze the strain induced emission enhancement factor, band structure is simulated with the 8 band *k·p* method, which is detailed in ref. [3], and spontaneous emission rates and absorption coefficients are calculated with the above elaborated joint density of state (JDOS) model.

Figure S4(a) is the strain-dependent band structure evolution of Ge, showing a reducing difference between the direct bandgap at Γ point and the indirect bandgap at L point, which will increase the electron population in the Γ valley, resulting in the spontaneous emission enhancement. Figure S4(b) shows the spontaneous emission rate of as-grown Ge and Ge microbridges. For the cases of ε_x = 1.6% and ε_x = 2.6%, the integrated spontaneous emission rates are 1.0×10^{21} $cm^{-3}s^{-1}$ and 3.0×10^{21} $cm^{-3}s^{-1}$, corresponding to enhancement factors of 2.4 and 7.3 comparing with the as-grown Ge. The calculated absorption coefficients of the as-grown Ge and Ge microbridge with uniaxial tensile strain of 2.6% are depicted in Fig. S4(c), comparing with the experimental data in ref. [4]. The main difference between the Ge microbridge and as-grown Ge is the edge of the absorption spectrum, locating at 2.1 μm and 1.6 μm, respectively.

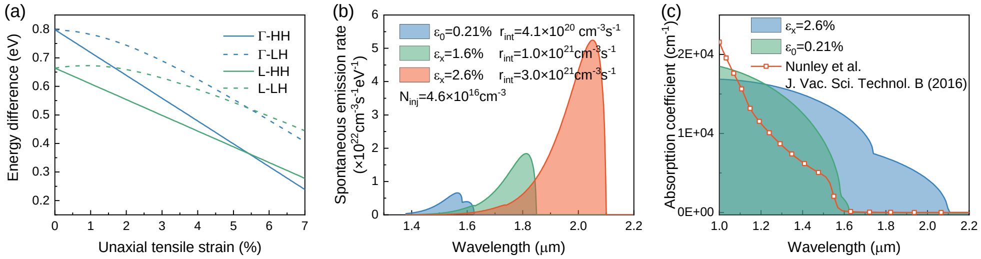

Figure S4. (a) Evolution of the band structure of germanium with uniaxial tensile strain. The energy differences between heavy hole (HH) and light hole (LH) and L, and direct bandgaps for HH and LH to Γ as the function of uniaxial tensile strain are calculated with the 8 band *k·p* method combined with the deformation potential theory. (b) Simulation of the spontaneous emission rate with the joint density of state (JDOS) model. Calculation for the as-grown Ge with biaxial tensile strain of 0.21% and Ge microbridge of uniaxial tensile strain of 1.6% and 2.6% are performed, with injected carrier density of 4.6×10^{16} cm^{-3}. (c) Calculated interband absorption for Ge with <100> uniaxial tensile strain of 2.6% or biaxial tensile strain of 0.21% in comparison to experimental data[4].

5. Calculation of electron statistics

The electron population is calculated by integrating the product of the density of states in the conduction band and the Fermi-Dirac function:

$$N_{\Gamma,L} = \int_{-\infty}^{\infty} \rho_{\Gamma,L}(E) f_c(E)\, dE \tag{S10}$$

$$\rho_{\Gamma,L}(E) = \frac{1}{2\pi^2}\left(\frac{2m^*_{\Gamma,L}}{\hbar^2}\right)^{3/2}\left(E - E_{\Gamma,L}\right)^{1/2}, E > E_{\Gamma,L} \tag{S11}$$

$$f_c(E) = \frac{1}{1 + \exp\left(\frac{E - \mu_e}{kT}\right)} \tag{S12}$$

Here, μ_e is the electron quasi-Fermi level. E_Γ and E_L are the strain-dependent band edge energies for the Γ and L valley, respectively. k is the Boltzmann constant, and T is the temperature. m_Γ^* is the derived strain-dependent effective mass of electrons in Γ valley via 8 band $k{\cdot}p$ method, while the m_L^* is assumed to be independent of strain.

6. Thermal stress and strain-enhancement factor related to dimensions

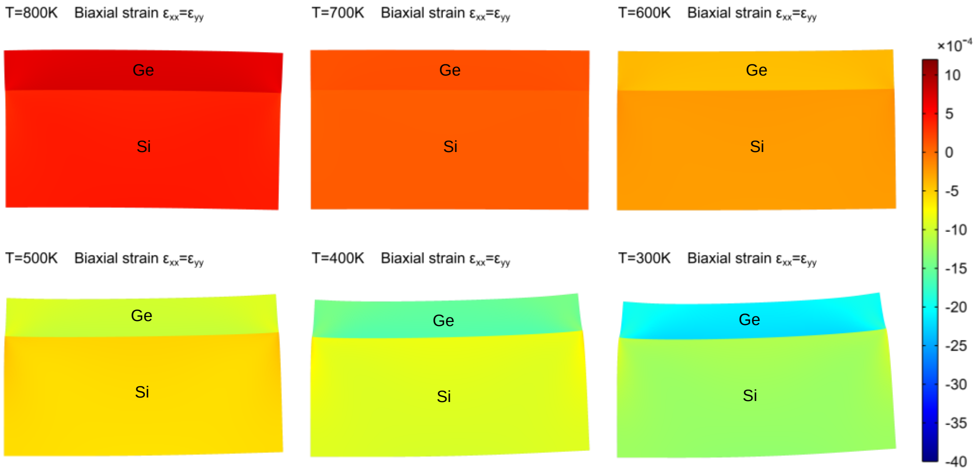

Figure S5. Evolution of strain in the as-grown Ge layer as cooling to room temperature, simulated with finite element method (FEM).

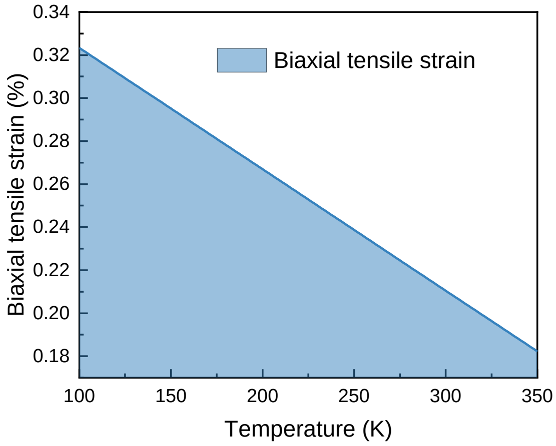

Figure S6. The biaxial tensile strain accumulation as cooling.

The Ge-on-SOI wafer used in this paper is grown at high temperature, with 400℃ (673.15K) for the buffer layer and 600℃ (873.15K) for the high-quality layer. When cooling to room temperature, biaxial tensile strain will generate in the Ge layer for its larger thermal expansion coefficient than Si. Figure S5 illustrates the simulated strain evolution in the as-grown Ge layer. As temperature decreases from 800K to 300K, the strain state of the material changes from the slight biaxial compressive strain (ε_0 = 0.05%) to the larger biaxial tensile strain (ε_0 = 0.2%). Figure S6 illustrates the biaxial tensile strain as a function of temperature from 100K to 350K. The strain value keeps accumulating as cooling.

Figure S7 depicts the strain concentration effect of the microbridge structure. The strain enhancement $\varepsilon_x/\varepsilon_0$, defined as the ratio of uniaxial tensile strain along the <100> direction ε_x divided by the biaxial strain ε_0 of the as-grown Ge layer, is related to the dimensions of the microbridge [5, 6]:

$$\varepsilon_x/\varepsilon_0 = C \times \left[1 + A/(B-A)\right] / \left[A/(B-A) + a/b\right] \tag{S13}$$

Here, A, B, a and b are structural parameters of microbridge as marked in Fig. S7. C is a correction factor to account for the influence of etching time and the waveguide on the bridge. In this paper, the strain parameter C is tuned by controlling the wet etching time for the bridge suspension to get different strain enhancement factor.

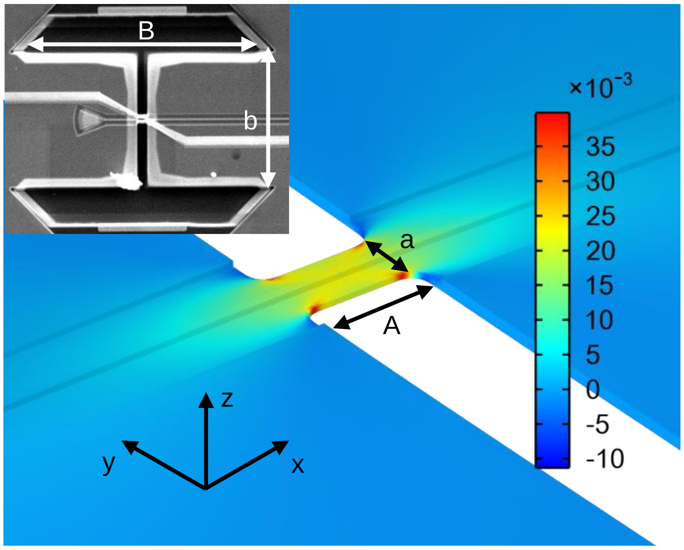

Figure S7. Uniaxial tensile strain ε_x in a Ge microbridge with ridge waveguide fabricated on it. Simulation is carried out with finite element method (FEM). The dimensions a, A, b, B refer to the width and length of the microbridge, the pad width and the whole length of a single microbridge structure, respectively. Inset: SEM picture of a single suspended microbridge.

7. Experimental schemes

A lock-in amplifier scheme is adopted in the test of the emitting-detecting configuration device. As presented in Fig. S8, the emitting part is powered by a function signal generator with a 1kHz square wave excitation signal. The duty cycle is tuned to 20% to reduce the average output power to protect the device under test (DUT). The detecting part is reversely biased by a digital source meter at the voltage of 0.2V. A resistance of 50 Ω is employed in the circuit to convert the photocurrent into a voltage signal. Since the photocurrent is on the order of microamperes, the reverse bias voltage fluctuation at the detecting end caused by the voltage change at both ends of the resistance is negligible. The signal generated at the detecting end is extracted from the noise by phase-sensitive detection with the lock-in amplifier. The DUT is placed on a thermo electric cooler (TEC) to adjust its temperature.

Electroluminescence (EL) test of the unsuspended device is also performed using the set-up shown in Fig. S9. The system is still based on a lock-in amplifier, with a function signal generator powering the emitting part with a 1kHz square wave signal. An object is placed above the grating coupler for the light collection. The light beam is focused on an InGaAs detector to convert optical signals into electrical signals. The electrical signals are sent to the lock-in amplifier and then output to the computer. The detector is fixed on a flip frame and can be easily flipped down to move out of the light path for the chip observation with a CCD.

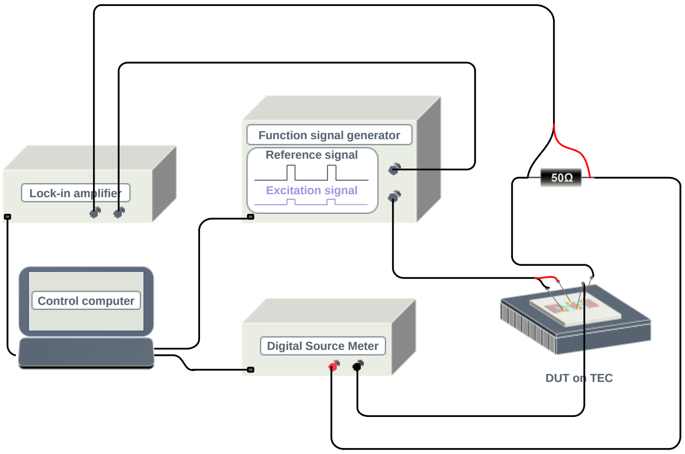

Figure S8. Schematic of the experimental set-up, highlighting the main elements: Lock-in amplifier, Function signal generator, Digital source meter, resistance of 50 Ω, device with emitting-detecting configuration under test on the thermo electric cooler (TEC).

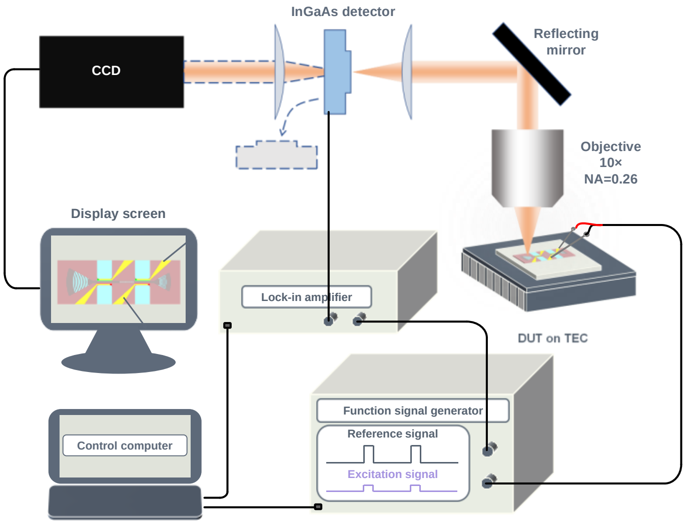

Figure S9. Schematic of the electroluminescence test set-up used in this work.

Figure S10(a)-S10(f) show the responsivity of the detector and transmissions of other components of the device and the EL system. The detector responsivity and transmissions of the objective and the planoconvex lens are given by their datasheets. The efficiency of the unsuspended grating coupler and the transmission of the surface grating are calculated with Finite Difference Time Domain (FDTD) method and Eigenmode Expansion (EME) method, respectively. The transmission of the 350 μm waveguide can be calculated according to the absorption coefficient of the as-grown Ge:

$$T(\lambda)=\exp\left(-\alpha(\lambda)L\right) \tag{S14}$$

Here, T is the waveguide transmission. λ is the wavelength. α is the absorption coefficient of the as-grown Ge shown in Fig. S4(c). L is the length of the waveguide.

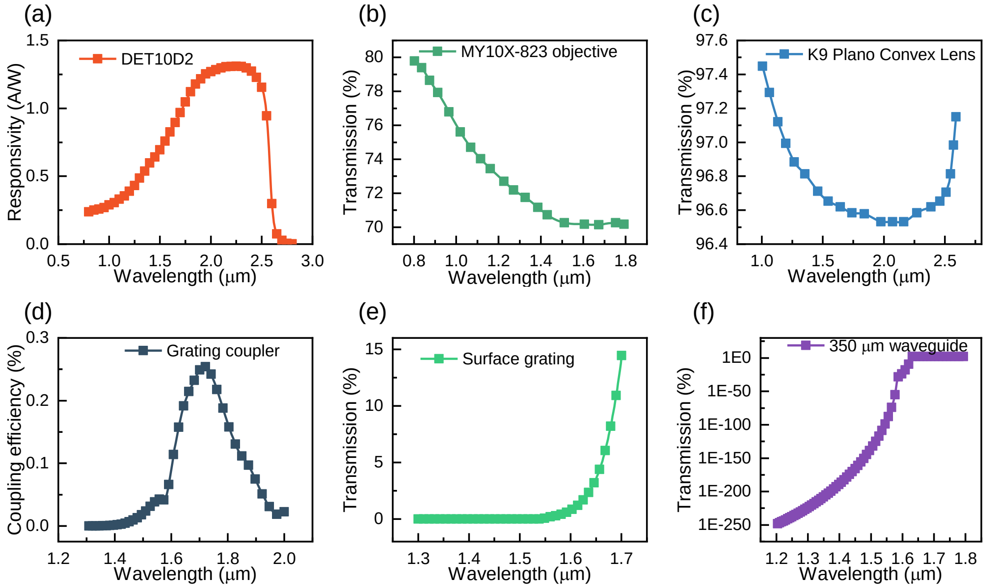

Figure S10. (a) Responsivity spectrum of the InGaAs detector. (b) Transmission of the long working distance Mitutoyo 0.26NA Near-IR objective. (c) Transmission of the K9 Plano Convex Lens. (d) Coupling efficiency of the grating coupler before suspension. (e) Transmission of the surface DBR grating. (f) Transmission of the waveguide with a length of 350 μm.

8. Reverse bias dependence of the detecting microbridge

The dependence of the detecting microbridge responsivity on the reverse bias voltage is explored. The test is performed on a device with uniaxial tensile strain of 2.6%, using the experimental set-up shown in Fig. S8. The reverse bias voltage of the detecting microbridge is tuned from 0V to 0.3V. The injected current of the emitting microbridge is fixed, as well as the light emission intensity. As shown in Fig. S11, the detecting output current is maintained between the range of 0.5 μA to 0.7 μA, with a fluctuation of 15%.

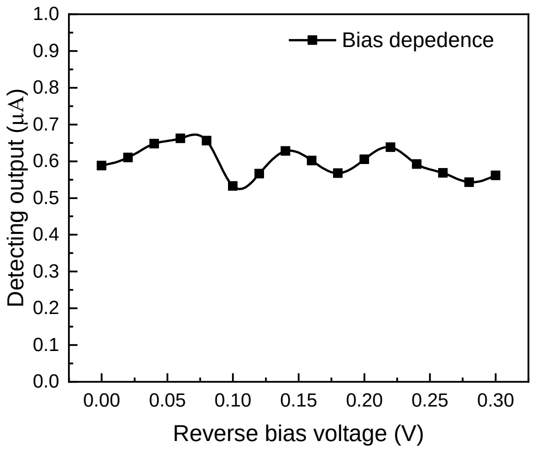

Figure S11. Output from the detecting microbridge as a function of the reverse bias voltage under a fixed current injected into the emitting microbridge.

9. Electrical circuit of the emitting-detecting test

The electrical circuit of the emitting-detecting test shown in Fig. S8 is illustrated in Fig. S12(a). The emitting diode D_1 is forward biased for light emission. D_2 is reversed biased to convert optical signals into current I_{PD}. R_s is the series resistance of the diode. A resistance 50 Ω is used to change I_{PD} into voltage signals. R_{load} is the load resistance of the lock-in amplifier.

There can be cross-talk between the emitting circuit and the detecting circuit due to the imperfect electrical insulation between the two different parts. To estimate such cross-talk, the electrical is changed as depicted in Fig. S12(b). The emitting diode D_1 is reversely biased to turn off the light emission, and there is only cross-talk electrical signals can be tested from the detecting part of the system. During the test, the output of the lock-in amplifier keeps fluctuating, and no effective data can be obtained, which means the cross-talk is smaller than the testing accuracy of the system and will not has influence on the testing results.

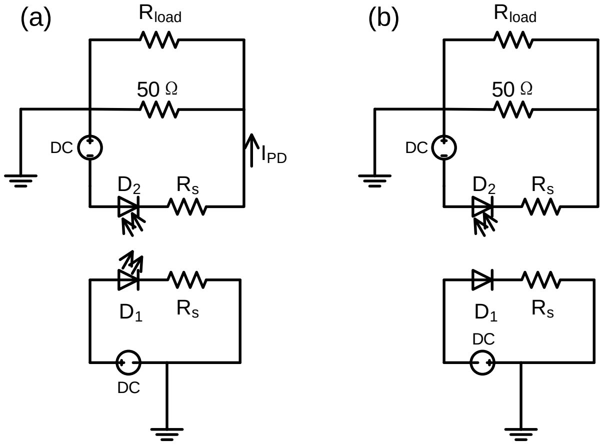

Figure S12. (a) The electrical circuit of the emitting-detecting test system, with the emitting microbridge forward biased. (b) The electrical circuit of the cross-talk test system, with the emitting microbridge reverse biased to prevent it from glowing.

10. Material inhomogeneity at the edge of the microbridge structure

As shown in Fig. S13(a), there are bright contrast regions around the microbridge structures, which is caused by the material inhomogeneity at the structure edge, displayed more clearly in the microscope image of Fig. S13(b). During the fabrication process, several SiO_x layer deposition and wet etching steps are performed. The deposition and etching rates at the edge regions are slightly different from the central area, which leads to the thickness difference of the SiO_x layer. Besides, gravity and stress in the structure will tilt the edges of the microbridge structure. These factors mentioned above contribute to the inhomogeneity at the edge of the microbridge structure.

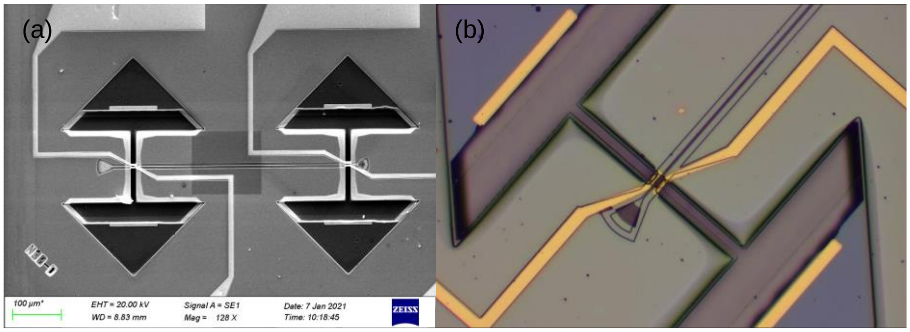

Figure S13. (a) SEM image of the device. (b) Microscope image of a suspended microbridge.

11. Material parameters used in the carrier density simulation

The calculation of the carrier density from the injected current density is performed using the finite element method. The material parameters used in the simulation are listed in Table S3, which are modified from the data in ref. [7] according to the strain value and doping concentrations.

Table S3. Material parameters used in the carrier density simulation

Parameters	p-region	active region	n-region
Band gaps (eV)	0.5280	0.5280	0.5280
Affinities (eV)	4.0189	4.0189	4.0189
Electron DOS effective masses (m_0)	0.1243	0.1243	0.1243
Hole DOS effective masses (m_0)	0.55	0.55	0.55
Electron mobilities ($m^2V^{-1}s^{-1}$)	0.0120	0.3900	0.0355
Hole mobilities ($m^2V^{-1}s^{-1}$)	0.0121	0.5655	0.0365
SRH lifetimes (ns)	3	3	3
Auger recombination coefficients C_{eeh} (cm^6s^{-1})	1.4×10^{-30}	1.4×10^{-30}	1.4×10^{-30}
Auger recombination coefficients C_{hhe} (cm^6s^{-1})	2×10^{-31}	2×10^{-31}	2×10^{-31}

12. References

1. R. Yujiao, C. Chengzhao, H. Shihao, H. Wei, C. Songyan, L. Cheng, and L. Jun, "Influence of implantation damages and intrinsic dislocations on phosphorus diffusion in Ge," IEEE Trans. Electron Devices **60**, 3741-3745 (2013).
2. A. Gassenq, S. Tardif, K. Guilloy, I. Duchemin, N. Pauc, J. M. Hartmann, D. Rouchon, J. Widiez, Y. M. Niquet, L. Milord, T. Zabel, H. Sigg, J. Faist, A. Chelnokov, F. Rieutord, V. Reboud, and V. Calvo, "Raman-strain relations in highly strained Ge: Uniaxial <100>, <110> and biaxial (001) stress," J. Appl. Phys. **121**, 055702-055710 (2017).
3. J. Jiang, M. Xue, C.-Y. Lu, C. S. Fenrich, M. Morea, K. Zang, J. Gao, M. Cheng, Y. Zhang, T. I. Kamins, J. S. Harris, and J. Sun, "Strain-induced enhancement of electroluminescence from highly strained germanium light-emitting diodes," ACS Photonics **6**, 915-923 (2019).

4. T. N. Nunley, N. S. Fernando, N. Samarasingha, J. M. Moya, C. M. Nelson, A. A. Medina, and S. Zollner, "Optical constants of germanium and thermally grown germanium dioxide from 0.5 to 6.6eV via a multisample ellipsometry investigation," Journal of Vacuum Science & Technology B, Nanotechnology and Microelectronics: Materials, Processing, Measurement, and Phenomena **34**, 061205-061213 (2016).
5. R. A. Minamisawa, M. J. Suess, R. Spolenak, J. Faist, C. David, J. Gobrecht, K. K. Bourdelle, and H. Sigg, "Top-down fabricated silicon nanowires under tensile elastic strain up to 4.5%," Nat. Commun. **3**, 1096-1101 (2012).
6. T. Zabel, R. Geiger, E. Marin, E. Müller, A. Diaz, C. Bonzon, M. J. Süess, R. Spolenak, J. Faist, and H. Sigg, "Top-down method to introduce ultra-high elastic strain," J. Mater. Res. **32**, 726-736 (2017).
7. J. Jiang, J. Sun, Y. Zhou, J. Gao, H. Zhou, and R. Zhang, "Design and analysis of a CMOS-compatible distributed Bragg reflector laser based on highly uniaxial tensile stressed germanium," Opt. Express **25**, 6497-6510 (2017).